Emergence of strong-coupling superconductivity and quantum criticality correlated with Lifshitz transitions in the alternate stacking compound $4H_b$-TaS$_2$

Shuxiang Xu [1,2,*], Junze Deng [1,*], Jingjing Gao,[3,*] Fanyu Meng [4,*], Lifen Shi,[1,5] Pengtao Yang,[1] Ningning Wang [1,5]
Ziyi Liu,[1,5] Jianping Sun [1,5], Yoshiya Uwatoko,[6] Hechang Lei,[4] Xuan Luo,[3] Yuping Sun,[7,3,8] Nanlin Wang [2]
Zhijun Wang,[1,5,9,†] Bosen Wang [1,5,9,‡] and Jinguang Cheng [1,5,§]

[1]*Beijing National Laboratory for Condensed Matter Physics and Institute of Physics, Chinese Academy of Sciences, Beijing 100190, China*
[2]*International Center for Quantum Materials, School of Physics, Peking University, Beijing 100871, China*
[3]*Key Laboratory of Materials Physics, Institute of Solid-State Physics, Chinese Academy of Sciences, Hefei 230031, China*
[4]*Department of Physics and Beijing Key Laboratory of Opto-electronic Functional Materials and Micro-nano Devices,
Renmin University of China, Beijing 100872, China*
[5]*School of Physical Sciences, University of Chinese Academy of Sciences, Beijing 100190, China*
[6]*Institute for Solid State Physics, University of Tokyo, Kashiwanoha 5-1-5, Kashiwa, Chiba 277-8581, Japan*
[7]*High Magnetic Field Laboratory, Chinese Academy of Sciences, Hefei 230031, China*
[8]*Collaborative Innovation Center of Microstructures, Nanjing University, Nanjing 210093, China*
[9]*Songshan Lake Materials Laboratory, Dongguan, Guangdong 523808, China*

$4H_b$-TaS$_2$ is a naturally formed quasi-two-dimensional heterojunction material composed of alternating monolayers of insulating ($1T$-) and superconducting ($1H$-) TaS$_2$. We report on a comprehensive high-pressure study on the interplay between charge-density wave (CDW) and superconductivity (SC) in $4H_b$-TaS$_2$. The results uncover a dome-shaped strong-coupling superconductor on the border of a 3×3 commensurate CDW at $P_{c1} \approx 2.0$ GPa: (1) nearly one order enhancement of upper critical field $B_{c2}(0)$; (2) the derived $2\Delta_0/k_B T_c$ beyond the BCS theory, decaying to a conventional one above 4.5 GPa; (3) the exponent of normal-state resistivity $n \approx 1.50$ and triply enhanced electronic effective mass. Under pressure, a third CDW emerging from 2.0 GPa is related to the original two CDWs, then disappears above 11.5 GPa. The temperature dependence of $B_{c2}(T)$ collapses into a universal curve and the comparison of $B_{c2}(T)$ to a polar-state function in $4H_b$-TaS$_2$. Theoretical calculations proposed the stronger interlayer coupling and band hybridization responsible for strong-coupling SC; the suppression of new CDWs is related to band inversions between the $1T$-Ta-d_{xy} (GM1+) and S-p_z bands (GM2-) at the ΓA point; above 5.0 GPa, the coexisting weak-coupling SC and linear magnetoresistance can be attributed to the formation of electronic bands along the M-K lines and the ΓA point. Our discovery provides an excellent example to demonstrate the interplay of the strong-coupling superconducting state and topological electronic state in van der Waals heterojunctions.

DOI: 10.1103/PhysRevB.109.144522

I. INTRODUCTION

Transition-metal dichalcogenides (TMDCs) with quasi-two-dimensional (Q2D) structures and weak van der Waals interlayer interactions have been the focus of extensive investigations in the recent years [1–7]. Its low-dimensional anisotropic structure and singular multiple Fermi surfaces offer an excellent platform to study the interplay of competitive and/or cooperative orders and unconventional superconductivity (SC) [8–13]. The easy exfoliation of some Q2D TMDCs offers opportunities to investigate the evolution of novel physical properties as a function of dimensionality and the number of stacking layers. In addition, in a fashion similar to the magic-angle graphene, the construction of artificial

heterostructures by stacking monolayers of different TMDCs has emerged as a fertile playground to explore emergent novel phenomena [4,5,9–20]. However, due to technological limitations and the instability of single-layer TMDC materials in air, it is difficult to study the relationship between CDW and SC in $1T$ and $1H$ monolayers under pressure [13,19]. Taking a step back, heterojunction materials with weak interlayer coupling might be a good research carrier.

As an example, $4H_b$-TaS$_2$ adopts a naturally formed Q2D heterostructure and displays interesting physical properties [14–17,21–28]. As depicted in Figs. 1(a)–1(c), its unique structure contains an alternative stacking of the monolayers of the $2H$- and $1T$-TaS$_2$ along the c axis [13–16]. Both $1T$- and $2H$-TaS$_2$ form a CdI$_2$-type structure but with a different coordination environment, i.e., the TaS$_8$ octahedron in the former versus the TaS$_6$ triangular prism in the latter [14,18,21]. In comparison with $1T$- and $2H$-TaS$_2$, the a axis remains unchanged while the c axis is greatly elongated in $4H_b$-TaS$_2$, which results in complicated anisotropic electronic structures and physical properties [14,15,22,23]. To illustrate
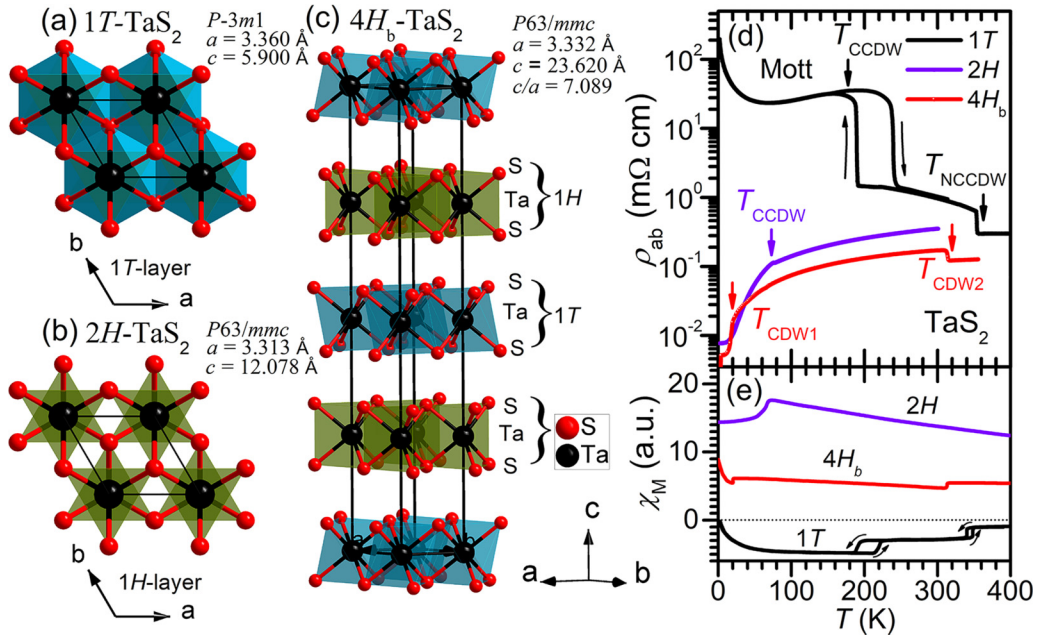
FIG. 1. (a)–(c) Crystal structures and lattice parameters (*a*, *c*, and *c/a*) of 1*T*-, 2*H*-, and 4*H_b*-TaS_2. Temperature dependence of (d) electrical resistivity $\rho(T)$ and (e) magnetic susceptibility are compared. The arrows indicate the CDW transitions.

this point, the temperature dependence of electrical resistivity of 1*T*-, 2*H*-, and 4*H_b*-TaS_2 was compared in Fig. 1(d). For 1*T*-TaS_2, it exhibits three successive charge-density waves (CDWs), i.e., an incommensurate CDW (ICCDW) at $T_{ICCDW} = 550$ K, a nearly commensurate CDW (NCCDW) at $T_{NCCDW} = 350$ K, and then a commensurate CDW (CCDW) at $T_{CCDW} = 190$ K, below which Ta atoms form star-of-David clusters with a $\sqrt{13} \times \sqrt{13}$ superlattice in the Mott insulating state of ∼0.3 eV [4,18–20]. For 2*H*-TaS_2, it shows only one 3×3 CCDW transition at $T_{CCDW} \approx 78$ K, prior to the SC at $T_c \approx 0.8$ K [29–34]. Interestingly, 4*H_b*-TaS_2 undergoes two CDW transitions: a $\sqrt{13} \times \sqrt{13}$ ICCDW at 315 K and a 3×3 CCDW at 22 K. At lower temperatures, 4*H_b*-TaS_2 becomes a superconducting state below $T_c \approx 2.7 - 3.7$ K, which is nearly triply enhanced compared to bulk 2*H*-TaS_2 [13–15,24–26,33–35]. The results indicate that the interlayer coupling of 1*T* and 1*H* monolayers is weak and the charge transfer between them can modify physical properties [14–16]. In this regard, it provides a good opportunity to study the interplay of CDWs and SC in a naturally formed heterostructure compound [27,28].

In terms of the SC observed in 4*H_b*-TaS_2, recent muon spin resonance has suggested it to be a chiral superconductor candidate due to the appearance of time-reversal symmetry breaking [15]. It was proposed that chiral SC is mediated by spin fluctuations close to a doped-Mott insulator and triangular gapless spin liquid [15]. The combination of angle-resolved microscopic transport and scanning tunneling microscopy (STM) reveals the presence of two-component SC and the chiral to nematic crossover of the superconducting state [16]. Possible pairing mechanisms including the mixed spin-singlet and spin-triplet states have been proposed. Similar to the electronic structures of 1*T*-TaS_2 [14,18], 4*H_b*-TaS_2 has narrow electronic bands near Fermi level due to the destruction of interlayer dimerization [14]. The STM

results showed the Mott gap of 1*T*-TaS_2 persists but shrinks to ∼30 meV, which originated from the intralayer electronic correlations [14,23]. However, the interplay of multiple CDWs and the chiral SC has not been studied.

The occurrence of a CDW is usually accompanied by symmetry breaking, lattice dimensionality crossover, and/or multiple entangled electronic states [36,37]. High pressure is a clean method to adjust structural and electronic properties of TMDCs [4,5,13,19,29–31,33]. Motivated by this, we chose the 4*H_b*-TaS_2 to reveal the evolution of CDWs and exotic SC [14,15]. By a palm-type cubic anvil pressure cell (CAC) [38,39], we report pressure-induced domelike strong-coupling SC on the border of CDW1 at $P_{c1} \approx 2.0$ GPa with enhanced upper critical field $B_{c2}(0)$, the exponent of resistivity $n \approx 1.50$, and the triply enhanced electronic effective mass. A third CDW emerges at $P_{c1} \approx 2.0$ GPa and changes its temperature-dependent resistivity derivative at $P_{c2} \approx 4.50$ GPa with a crossover from strong- to weak-coupling SC by the quick reduction of $2\Delta_0/k_B T_c$. Theoretical calculations reveal the existing strong interlayer coupling and band hybridization is responsible for strong-coupling SC. The emerged CDW transition starting from P_{c1} is suppressed by band inversions between the 1*T*-Ta-d_{xy} (GM1+) and S-p_z bands (GM2-) at the ΓA point.

II. EXPERIMENTAL METHODS

Single-crystal 4*H_b*-TaS_2 was grown by the iodine transport method [14,15]. Details of crystal growth and physical properties at ambient pressure (AP) are summarized in the Supplemental Material (Figs. S1 and S2) [40]. Both single-crystal and powder x-ray diffraction confirm the high quality of 4*H_b*-TaS_2 (space group *P63/mmc*, No. 194). The piston-cylinder pressure cell (PCC) and CAC were employed to measure resistivity and Hall conductivity up to 11.5 GPa [38,39].

Glycerol is used as the pressure transmitting medium. Pressure in the CAC was estimated from the calibration curves predetermined via measuring structural transitions of bismuth at room temperature and the superconducting transition of Pb at low temperatures. $P(T)$ was measured by a standard four-probe method with the current parallel to the ab plane and the applied field to the c axis. ac susceptibility under pressure was collected with a mutual reduction method at a frequency of 307 Hz under a small modulation field parallel to the ab plane [38]. All the experiments were performed in a ^{4}He refrigerated cryostat (1.4 K $\leqslant T \leqslant$ 295 K and 0 T $\leqslant H \leqslant$ 9 T).

First-principles calculations were performed based on the density functional theory (DFT) using the projector augmented wave method [41,42] implemented in the Vienna *ab initio* simulation package (VASP) [43,44] to obtain the electronic structures and Fermi surfaces of materials. The generalized gradient approximation with the exchange-correlation functional of Perdew, Burke, and Ernzerhof [45] was adopted. The kinetic energy cutoff was set to 400 eV for the plane wave basis. The Brillouin zone was sampled by the Γ-centered Monkhorst-Pack method [46] with a $12 \times 12 \times 1$ **k** mesh for the three-dimensional periodic boundary conditions in the self-consistent process. The irreducible representations of electronic states are obtained by IRVSP [47].

III. RESULTS AND DISCUSSIONS

A. Evolution of the CDW phase transitions under high pressure

Figures 2(a)–2(c) show the $\rho(T)$ of $4H_b$-TaS$_2$ (1#,2#) under various pressures. At AP, $\rho(T)$ retains a metallic behavior in 2–300 K except for a small drop of $\sim$10 $\mu\Omega$ cm at 22 K and an upturn of $\sim$16 $\mu\Omega$ cm at 315 K, which correspond to CDW1 and CDW2, respectively. Here, the T_{CDW1} and T_{CDW2} are defined as the peak in the $\rho(T)/dT$ in Fig. S3 and marked in Figs. 2(a)–2(c). The formation of CDW1 produces a strong anisotropy of resistivity (Fig. S2), e.g., the ab-plane resistivity suddenly decreases while the out-of-plane resistivity (nearly 200 times larger) firstly increases due to the gap opening on the Fermi surface and then decreases upon further cooling [14]. Magnetic susceptibility increases steeply accompanying the sharp fall of the ab-plane resistivity at 22 K [20,32] [Figs. 1(d) and 1(e)], in contradiction with common features [3,32]. Such a CDW has been argued to be closely connected with the slightly doped-Mott insulating 1T monolayer [4,15,33,34]. We note that the coupling between two CDWs is weak at AP, which motivates us to achieve exotic electronic behaviors through high-pressure regulation of interlayer couplings.

With increasing pressure, CDW1 and CDW2 exhibit different pressure dependence. For 3×3 CDW1, the phase transition broadens up and the drop in $\rho(T)$ becomes smaller with pressure; the T_{CDW1} increases slightly and then cannot be detected in the $\rho(T)$ above 1.93 GPa in Figs. S3(a)–S3(c) and S3(e); the normal-state resistivity ($T_c \leqslant T \leqslant$ 40 K) firstly increases until 1.93 GPa and then decreases to one-tenth above 5.0 GPa in Fig. 2(c). The changes in these parameters imply the pressure-induced collapse of CDW1. However, it looks like CDW1 undergoes a first-order transition, which is different from the second-order 3×3 CDW transition in bulk 2H-TaS$_2$. For the CDW2, it is gradually restrained from
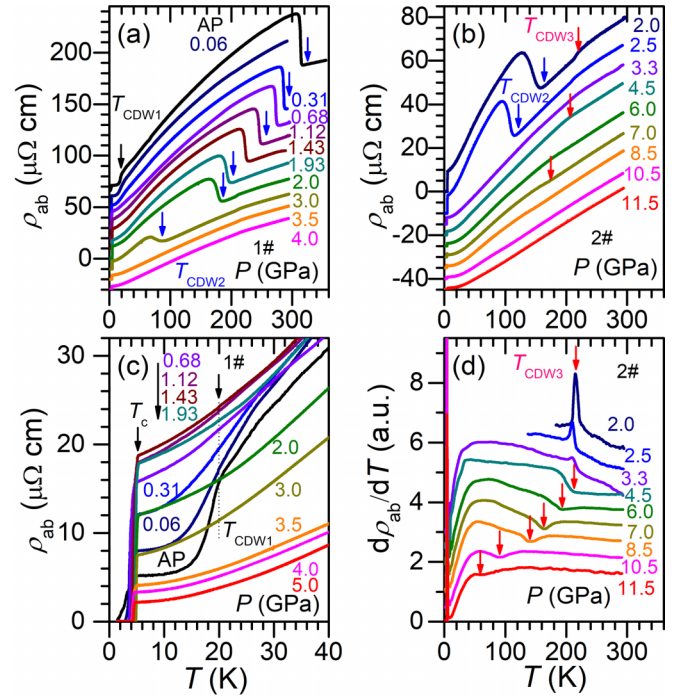

FIG. 2. (a)–(c) $\rho(T)$ in a PCC and a palm-type CAC for $4H_b$-TaS$_2$ (1#,2#). The data in (a) and (b) are shifted a constant along the longitudinal coordinate for comparison. (d) The derivation $d\rho(T)/dT$ to map the evolution of the CDW transition; it changes from a sharp peak to a broad trough at 4.50 GPa. All three CDW transitions and the superconducting transition are marked by T_{CDW1}, T_{CDW2}, T_{CDW3}, and T_c, respectively.

315 K at AP to $\sim$190 K at 1.93 GPa, and then disappears at $P_{C2} \approx$ 4.50 GPa as shown in Figs. 2(b)–2(c), which implies the collapse of CDW2 upon compression. Interestingly, except for these two explicit CDWs, some weak signals at high temperatures in $\rho(T)$ and $d\rho(T)/dT$ for 1# and 2# can be observed in Figs. 2(a) and 2(b). For example, $\rho(T)$ shows a clear kink and $d\rho(T)/dT$ exhibits a sharp peak starting from $\sim$200 K at 2.0 GPa, which indicates the emergence of a third CDW. Meanwhile, upon compression, the kink in $\rho(T)$ at $P \leqslant$ 3.30 GPa transforms into a broad shoulder for $P \geqslant$ 4.50 GPa; accordingly, $d\rho(T)/dT$ becomes a broad trough for $P \geqslant$ 4.50 GPa, which coincides with the critical pressures for the collapse of CDW2. On further compression, CDW3 reduces rapidly and starts to collapse above 11 GPa. However, the mechanism of CDW3 is unclear.

B. Evolution of the superconducting transition with pressure

In addition to following the evolution of CDWs, the superconducting transition is tracked by monitoring the onset and zero-resistivity transition temperatures, T_c^{onset} and T_c^{zero}, which show nonmonotonic pressure dependence. As in Fig. 3(a), T_c^{onset} and T_c^{zero} are enhanced firstly up to $\sim$5.42 and 4.55 K at $P_{c1} \approx$ 2.0 GPa and then reduced to $\sim$4.54 and 4.08 K at $P_{C2} \approx$ 4.50 GPa. Upon compression, both remain nearly constant with a slight increase accompanying the collapse of CDW3 for $P \geqslant$ 11 GPa. The resistivity jump at the superconducting transition as a function of temperature and field near $P_{c1} \approx$ 2.0 GPa is approximately five times larger
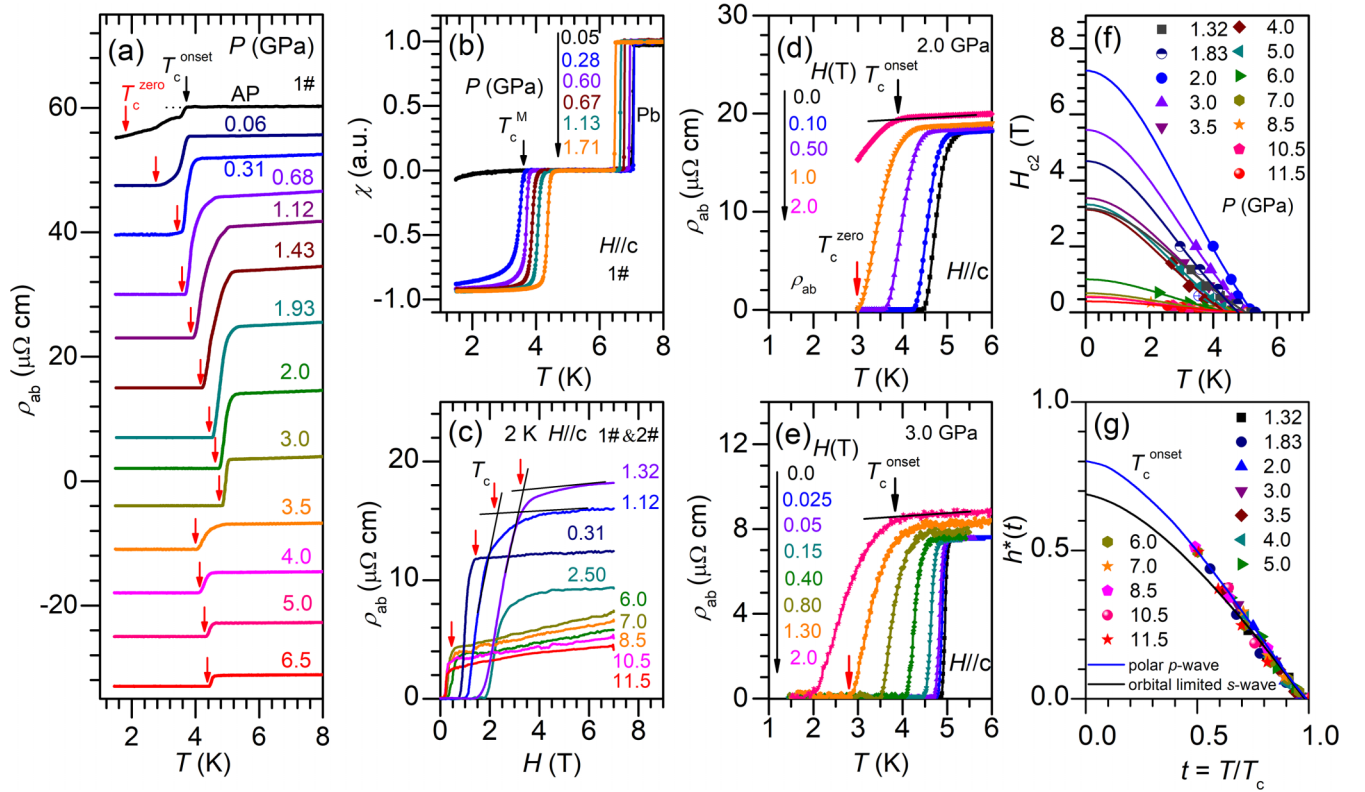
FIG. 3. (a) $\rho(T)$ below 8 K for $4H_b$-TaS$_2$ (1#); the arrows indicate T_c^{onset} and T_c^{zero}, respectively. (b) T dependence of ac susceptibility in PCC. (c) H dependence of resistivity at 2 K in PCC and CAC. The across points are defined as superconducting transition temperature. The H dependence of $\rho(T)$ below 6 K under various pressures and magnetic fields: (d) 2.0 GPa and (e) 3.0 GPa. The T dependence of the upper critical field of $B_{c2}(T)$. The $B_{c2}(0)$ was extracted by the WHH model, viz., $B_{c2}(T) = B_{c2}(0)[(1-t) - C_1(1-t)^2 - C_2(1-t)^4]/0.73$ with $C_1 = 0.135$ and $C_2 = 0.134$, respectively. (d) The normalized upper critical field $h^* = B_{c2}(0)/T_c [(-dB_{c2}/dT)_{T_c}]$ versus the reduced temperature $t = T/T_c$, and the fittings by an orbital limited s wave and a polar-state function, respectively.

than those at AP and 6–11.5 GPa in Figs. 3(a) and 3(c), implying these distinct superconducting states. As shown in Fig. 3(b), we measured temperature-dependent ac susceptibility $4\pi\chi_v(T)$ reflecting the superconducting shielding volume fraction. $4\pi\chi_v$ (2 K) increases in jumps from zero at low P (e.g., AP, 0.05 GPa) to nearly 1 at 0.28–1.71 GPa. This suggests that the interlayer coupling strength between $1T$ and $1H$ layers is weak at AP, and thus bulk SC is absent [38]. A small amount of pressure increases the interlayer coherence of Cooper pairs and charge transfer, resulting in bulk SC.

Based on these results, we constructed phase diagrams of CDWs and SC in Fig. 4(c). Along with the collapse of CDW1, the domelike SC phase appears, reaching a maximum of $T_c^{\max} \approx 5.42$ K near ≈ 2 GPa; however, the T_c is weakly affected by the collapse of CDW2 around ≈ 4.50 GPa, which is consistent with the assertion that SC mainly comes from $1H$ layer. Our results suggest that the critical fluctuations close to the collapse of CDW1 may provide pairing glue for SC [14–16,20,36,37].

C. Pressure dependence of the normal-state properties

Due to the limited sensitivity of electrical transport to detect CDWs, it is difficult to find the weak or short-order CDW with reduced CDW correlation length. Previous literature has used an empirical formula to extract the putative critical pressure for the vanishing of CDWs, which produces results

consistent with the experiments. In this work, the T_{CDW2} and T_{CDW3} were fitted by the empirical formula, viz., $T_{\text{CDW}}(P) = T_0(1 - P/P_c)^\beta$, where T_0, P_c, and β represent the T_{CDW} at AP, the critical pressure where the T_{CDW} reduces to zero, and the pressure exponent characterizing the suppression of CDW, respectively [13,19]. For CDW2, the best fitting yields the $T_0 \sim 322.15$ K, $P_c \sim 4.51$ GPa, and $\beta \sim 1.05$, respectively. For CDW3, the fittings give $T_0 \sim 245.41$ K, $P_c \sim 12.38$ GPa, and $\beta \sim 0.521$, respectively. The distinct values of β for CDW2 and CDW3 indicate different mechanisms.

Generally, the normal-state resistivity just above the T_c can reflect some information of the superconducting state, such as the effective mass and electron correlation strength. To further understand the T-P phase diagram, we quantitatively analyzed the resistivity just above the T_c by $\rho = \rho_0 + AT^n$ in Figs. 4(a) and 4(b), where ρ_0 represents the residual resistivity, and the quadratic coefficient $A(n = 2)$ and n positively correlate the density of states at Fermi level $N(E_F)$ and inelastic electron scatterings, respectively [5,19,36]. A polynomial fitting for $T_c < T < 20$ K gives the $\rho_0(P)$ and $n(P)$ and a linear fitting for $n = 2$ yields the $A(P)$. The temperature range of 2–20 K are empirical considering that phonon contributions in this temperature range should be reduced to a small level or remains unchanged as a function of pressure. Conversely, it is unfavorable for analyzing experimental results at high temperatures when phonon scattering becomes greater. In Fig. 4(d),
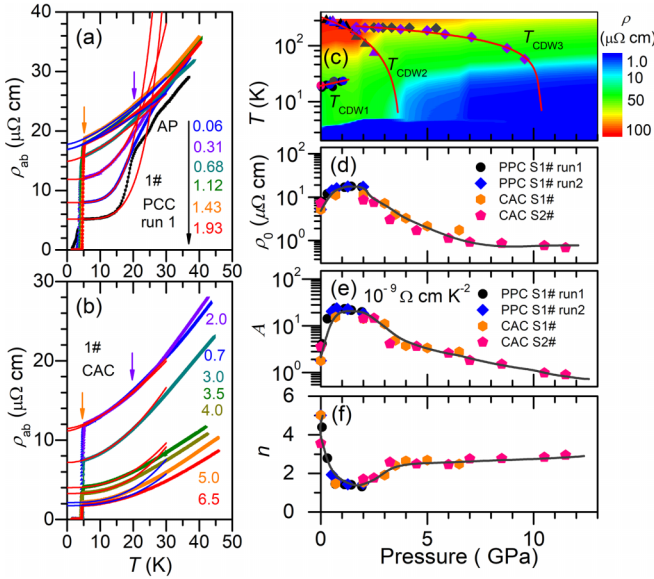
FIG. 4. Normal-state resistivity just above the T_c and its polynomial fitting by $\rho(T) = \rho_0 + AT^n$ in a range of $T_c^{onset} \leqslant T \leqslant 20$ K for $4H_b$-TaS$_2$: (a) PCC run1, 1# and (b) CAC, 1#. (c) The P dependence of CDW transitions; the solid lines indicate the trends. The pressure dependence of T_{CDW2} and T_{CDW2} was the fittings by $T_{CDW}(P) = T_0(1-P/P_c)^\beta$, where the T_0, P_c, and β represent T_{CDW} at AP, the critical pressure for the collapse of CDW, and the exponent characterizing the suppression of CDW, respectively. The P dependence of characteristic parameters: (d) the residual resistivity ρ_0, (e) the temperature coefficient A, and (f) the exponent n. The A is linearly fitted with $\rho(T) = \rho_0 + AT^2$. The black solid lines show the trends.

ρ_0 increases up to a maximum (18 μΩ cm) at P_{c1}, about four to five times larger than AP (4.8 μΩ cm) and reduces to less than 1 μΩ cm above P_{c2}. In a similar manner, in Fig. 4(e), $A(P)$ enhances to nearly an order of magnitude higher than AP at P_{c1}, shows a long tail near P_{c2}, and then is nearly zero for $P \geqslant 6.0$ GPa. The positive correlation between $A(P)$ and $T_c(P)$ suggests that the enhanced $N(E_F)$ or effective electronic mass at P_{c1} is responsible for the enhancement of T_c [5,29,48]. In Fig. 4(f), the n(AP) initially decreases from ~5.0 for phonon scatterings at AP to a minimum ~1.30 for a non-Fermi liquid at P_{c1}, and then recovers to ~1.95 at 3.0 GPa for a Fermi liquid before reaching ~3.0 at 11.5 GPa. The initial reduction of n can be taken as the hallmark for the critical fluctuations [5,13,19]. Our results confirm the close relationship of the enhanced T_c and the collapsed CDW1 at $P_{c1} \approx 2.0$ GPa. Moreover, the dependence of characteristics basically confirms the critical pressure where CDW1 disappears is a quantum critical point and the sudden disappearance of CDW1 is due to the inability of resistivity to detect CDWs.

To deeply understand the superconducting diagram, the T and H dependence of magnetoresistance MR$(T, H)(=[\rho(T,H) - \rho(T,0)/\rho(T,0)])$ was investigated. As shown in Figs. 5(a) and 5(b) and S5, all the MR(T,H) are positive below 50 K, originating from the high mobility of hole-type carriers and partial compensation [14,26]. Up to 11.5 GPa, two different pressure and temperature trends of MR are revealed: the MR at 10 K and 7.0 T is ~74% at AP, reduces to ~22% at 1.12 GPa, and shows a significant double increase to 48% near
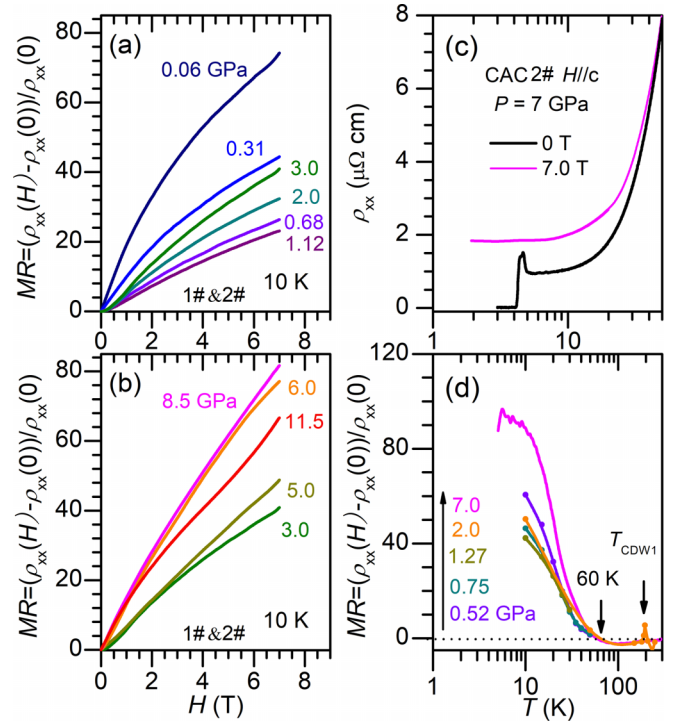

FIG. 5. Field dependence of MR under various pressures at 10 K in the range of (a) 0.06–3.0 GPa and (b) 3.0–11.5 GPa, respectively. (c) Temperature dependence of electrical resistivity was investigated under 0 and 7.0 T at a fixed pressure of 7.0 GPa. (d) The estimated MR based on the data in Fig. S5 and (c) under various pressures. The arrows indicate the CDW transition with an enhanced positive MR and 60 K where the MR≈0.

$P_{c1} \approx 2.0$ GPa, and then recovers to 62% about 11.5 GPa; the H dependence MR(H) at 10 K shows a crossover from $H^{1/2}$ dependence below 5.0 GPa to H dependence at 5–11.5 GPa, which indicates the collapse of CDW1 [2,3,26,29–31]. In Fig. 5(c), the temperature dependence of electrical resistivity was investigated under 0 and 7.0 T at a fixed pressure of 7.0 GPa and the estimated MR was summarized based on the data in Figs. 5(a)–5(c) and S5 under various pressures. We can find that the MR$(T,7.0$ T) at 7.0 GPa increases from −2% above 60 K (the MR≈0) to a maximum ~90% at 10 K; an enhanced positive MR up to 5.8% ($H = 7.0$T) is observed around the CDW transition, which may be attributed to the temperature-dependent change of energy bands. Based on these results, the coexisting linear MR and weak-coupling SC above 5.0 GPa makes $4H_b$-TaS$_2$ possible topological superconductors with nontrivial electronic states [14–17,23,24,49]. To get more electronic structures, Hall resistivity $\rho_{xy}(H)$ and Hall conductivity $\sigma_{xy}(H)$ were investigated at 10 K under pressure in Figs. 6(a) and 6(b). It stays negative, reduces to a minimum at P_{c2}, and then continues to increase until 6.50 GPa, implying the changes of carrier concentration and larger variations in Fermi surface. Its nonlinear H dependence is the signature of multibands of electronic structures [14–17]. The $\sigma_{xy}(H)$ was plotted in Fig. 6(b) and analyzed by a two-band model [14,40,49,50]:

$$\sigma_{xy} = \rho_{xy}/[(\rho_{xy})^2+(\rho_{xx})^2] = \left(\frac{n_h\mu_h^2}{1+(\mu_hB)^2} - \frac{n_e\mu_e^2}{1+(\mu_eB)^2}\right)eB.$$
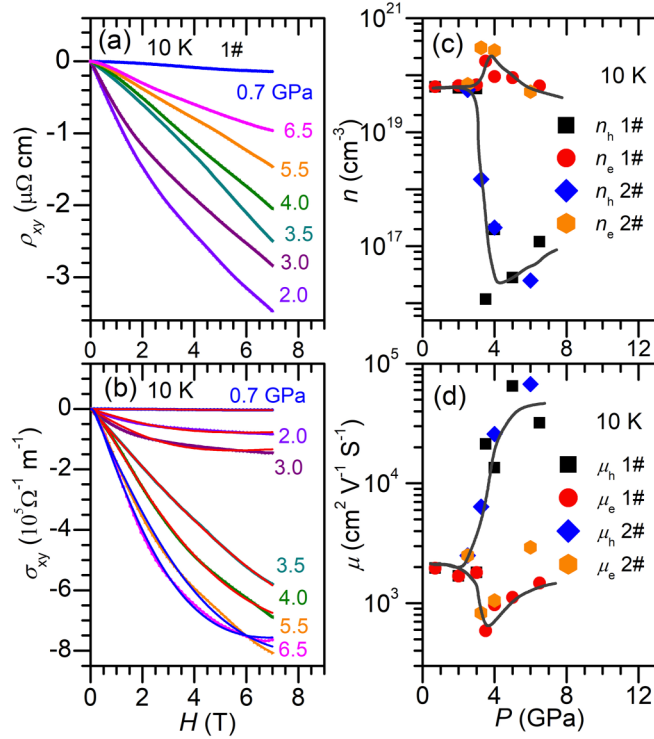
FIG. 6. (a) Hall resistivity $\rho_{xy}(H)$ of $4H_b$-TaS$_2$ at 10 K under pressure; (b) Hall conductivity $\sigma_{xy}(H)$ at 10 K and the mathematical fittings by the two-band model. Pressure dependence of characteristic parameters at 10 K: (d) carrier concentration, the electron-type n_e, and the hole-type n_h; (d) the mobility, the μ_e, and μ_h, respectively. Solid lines across the experimental data indicate the changing trends.

Here, the n_e, μ_e, and n_h, μ_h represent the concentration and the mobility of electron- and hole-type carriers, respectively. $\sigma_{xy}(H)$ was well fitted and the derived parameters were summarized in Figs. 6(c), 6(d), and 7: the n_e and n_h are equal as the features of compensating metal or semimetal; the slightly increased n_e exceeds the three times reduced n_h and electron-type carriers are dominated above 2.50 GPa; accordingly, the μ_h enhances abruptly with nearly 40 times enhancement above 5.0 GPa while the μ_e varies slightly, which implies pressure-driven Fermi surface reconstruction [51–53].

D. Pressure dependence of superconducting-state properties

To get more information on superconducting phases, $\rho(T)$ were measured under different fields in Figs. 3(d), 3(e), and S6(a)–S6(l). Using the criteria of T_c^{onset} and T_c^{zero}, the upper critical field $B_{c2}(0)$ was extracted in Fig. 3(f) by the Werthamer-Helfand-Hohenberg (WHH) model, viz., $B_{c2}(T) = B_{c2}(0)[(1-t) - C_1(1-t)^2 - C_2(1-t)^4]/0.73$ with $C_1 = 0.135$ and $C_2 = 0.134$, respectively [54]. In Fig. 7(b), $B_{c2}(0)$ enhanced up to a maximal $B_{c2}(0)^{\text{max}} \sim 7.37$ T at 2.0 GPa and then decreased to 3.31 T at 5.0 GPa. $B_{c2}(0)^{\text{max}}$ is nearly one order larger in magnitude than those at AP and 6–11 GPa where $B_{c2}(0) \sim 0.35$–0.55 T although T_c is as high as 4.55–5.10 K. Generally, the slope of the normalized $B_{c2}(0)$ by T_c is related to Fermi velocity and superconducting gap symmetry [55,56]. Accordingly, the P dependence
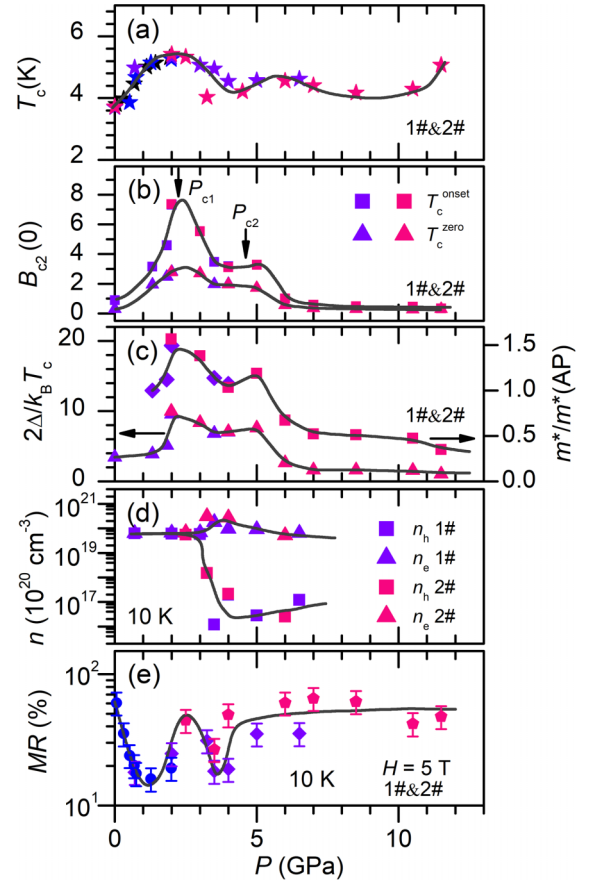

FIG. 7. The characteristic parameters of normal/superconducting state: (a) T_c^{onset}; (b) $B_{C2}(0)$; (c) the normalized $2\Delta(0)/k_B T_c$ and effective electronic mass $m^*/m^*(\text{AP})$; (d) the electron- and hole-type carriers concentration; (e) the MR (10 K) at 5.0 T under pressure. The solid lines across the data indicate the changing trends.

of $-(1/T_c)/[dB_{c2}(0)/dT]|_{T_c}$ exhibits a broad peak at $P_{c1} \approx 2.0$ GPa with triple enhancement compared to those at AP and above 5.0 GPa. To figure out a possible superconducting mechanism, we examined the gap symmetry by plotting the normalized upper critical field $h^* = B_{c2}(0)/T_c$ $[(-dB_{c2}/dT)_{T_c}]$ versus the reduced temperature $t = T/T_c$ in Fig. 3(g). All the points collapse into one well-defined curve, giving evidence that the superconducting gap symmetry remains unchanged [55,56]. However, the data deviates from a standard orbital limited s wave for the spin-singlet state but close to a polar-state function pointing to partial spin-triplet pairing, in accordance with time-reversal symmetry breaking in $4H_b$-TaS$_2$ [14–17]. However, the use of the temperature dependence of the upper critical field to deduce an unconventional superconducting state is not enough because an unusual temperature dependence of the upper critical field may originate from Fermi surface properties and weak gap anisotropy in some conventional s-wave superconductors.

Moreover, the superconducting coupling strength $2\Delta(0)/k_B T_c \approx B_{c2}(0)/(T_c A^{1/4})$ was roughly estimated by $B_{c2}(0) \approx 2\Delta(0)[\pi N(E_F)]^{1/2}$ and $N(E_F) \sim A^{1/2}$ [49,55–57]. In Fig. 7(c), with increasing P, the normalized $2\Delta(0)/k_B T_c$ is enhanced slightly to a maximum at P_{c1}, and then reduced rapidly to near constant for $P \geqslant 5.0$ GPa. For comparison,
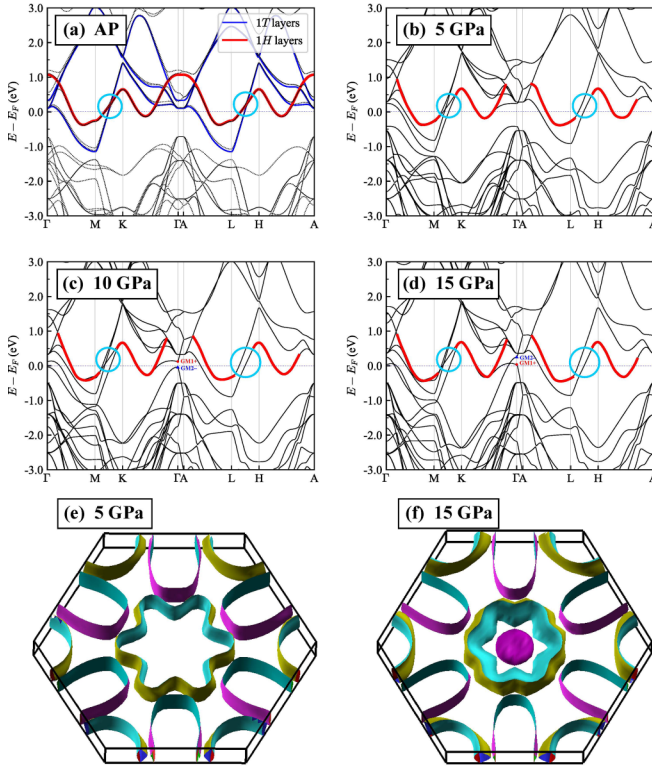
FIG. 8. The electronic band structures from first-principles calculations for (a) AP, (b) 5 GPa, (c) 10 GPa, and (d) 15 GPa. The dashed lines in (a) are the band structures of $4H_b$-TaS_2. The Brillouin zone and Fermi surfaces for (e) 5.0 and (f) 15 GPa, respectively. We note that the new hole pocket emerges at 15 GPa in the ΓA points.

$2\Delta(0)/k_B T_c \approx 3.435$ for $4H_b$-TaS_2 indicates weak-coupling or moderate-coupling SC at AP by the measured $\Delta(0) \approx 0.40$ meV [15–17]. Interestingly, the estimated $2\Delta(0)/k_B T_c$ are as large as ≈ 9.6 at $P_{c1} \approx 2.0$ GPa and show strong-coupling SC, and then reduced to 1.732 for weak-coupling SC at $P \geqslant 5.0$ GPa. Moreover, the effective electronic mass $m^*/m^*(AP)$ (the $m^* \sim n^{1/3}[dH_{c2}(T)/T_c dT_c]^{0.5}$) [49,55–57] in Fig. 7(c) shows a similar broad peak at $P_{c1} \approx 2.0$ GPa, indicating a dramatic variation of electron correlations near P_{c1}. Finally, the enhanced $B_{c2}(0)$, $2\Delta(0)/k_B T_c$, and $m^*/m^*(AP)$ at P_{c1} compared to those at AP and 5.0–11.5 GPa involve superconducting coupling strength, e.g., for $4H_b$-TaS_2, low-P SC is classified as strong coupling and turns into weak coupling at 5–11.5 GPa [3,40,49,57,58]. Such phenomenon has been observed in iron-based and heavy fermion superconductors [10,11,40,49].

E. Theoretical calculations and discussions

From the above analyses, the emergent strong-coupling SC and the evolution of $B_{c2}(0)$ and $m^*/m^*(AP)$ cannot be ascribed to the change of superconducting gap symmetry. To further substantiate this point, we performed DFT calculations on electronic structures of $4H_b$-TaS_2 at pressures AP, 5, 10, 15 GPa in Fig. 8. There are two bands crossing the Fermi level: one doubly degenerate band colored in blue is from $1T$ layers, while the doubly degenerate band colored in red is from $1H$ layers. As depicted in Fig. S7, the bands of $4H_b$-TaS_2

are similar to the simple summation of $1H$ (red bands) and $1T$ layers (blue bands) separately, indicating the interlayer coupling is weak at AP. Thus, at AP, the interband scatterings do not open an energy gap in the M-K and L-H lines but bring on a complex and crumpled Fermi surface with both electron and hole pockets, which supports Fermi surface nesting and CDW formation. After applying pressure, the interlayer coupling and band hybridization become stronger, which would significantly change the Fermi surfaces. Usually, this change can suppress the CDW from $1H$ and $1T$ phases, and reduce the T_{CDW1} ($1H$) and T_{CDW2} ($1T$), respectively. In this regard, the corresponding enhanced interband scatterings of the $1T$ and $1H$ layers are important and may favor strong-coupling SC along with the collapse of CDWs at $P_{c1} \approx 2.0$ GPa, perfectly consistent with the above observations. Moreover, the previous STM results have shown that the Mott gap of $1T$-TaS_2 monolayer still persists but shrinks to ~ 30 meV, which mainly originates from the intralayer electronic correlations. It indicates that the Mott phase in monolayer should be relatively weak, and on the contrary, interlayer charge transfer is important, in good agreement with our DFT calculations. In addition, the calculations are consistent with experimental results, indicating that the interlayer coupling variation trend derived by DFT is reasonable. However, we should note that the trends in the interlayer coupling deduced from DFT are reasonable despite the difficulties of capturing the Mott physics using DFT.

With further compression, the simultaneously enhanced charge transfer from $1T$ to $1H$ layers reconstructs the Fermi surface or weakens the Fermi surface nesting [14]. In Figs. 8(b)–8(d), up to 5.0 GPa, $1T$-layer bands in the M-K and L-H lines move down rapidly and weaken the interlayer coupling band hybridization; at the same time, new electronic bands generate at 5.0 and 10 GPa in the M-K lines. The degenerate electronlike pocket at AP is split into topological bands and the interband scattering gets weaker, coinciding with the observed crossover of strong- to weak-coupling SC at 5.0 GPa. Accordingly, the coexistence of linear MR and weakly coupled SC is a feature of the appearance of topological electronic states near Fermi level in $4H_b$-TaS_2 [14–16,40,50,52]. Such unusual behaviors emerge in topological superconductors and semimetals [49,50,52,59–61].

On further compression to 15 GPa, we find that a new hole pocket emerges at the ΓA points, and these bands broaden at the expense of density states at E_F in Figs. S7(e)–S7(h). As a result, these bands near the ΓA points show weaker dispersion transitioning from a hole-type pocket to an approximate flat band near the Fermi level, which is dominated by the electron-type carriers as indicated in Figs. 6 and 7(d). Accordingly, the emerged T_{CDW3} in $4H_b$-TaS_2 is suppressed by band inversions between the $1T$-Ta-d_{xy} (GM1+) and S-p_z bands (GM2−) at the ΓA points, which happened near E_F at 10–15 GPa. Finally, our DFT calculations demonstrate the importance of interband scattering for the emerged strong-coupling SC at $P_{c1} \approx 2.0$ GPa; the coexistence of the weak-coupling SC and linear MR above 5.0 GPa is accompanied by the formation of new electronic bands along the M-K lines and the ΓA points. More in-depth studies need further detailed theoretical calculations and microscopic experimental explorations.

IV. CONCLUSION

We report a dome-shaped strong-coupling SC on the border of a 3×3 CDW1 at $P_{c1} \approx 2.0$ GPa with enhanced upper critical field $B_{c2}(0)$ and $2\Delta_0/k_B T_c$ beyond the BCS theory. The collapse of CDW1 is manifested by the reduced exponent $n \approx 1.50$ at 2.0 GPa and enhanced m^*/m^*(AP). The temperature dependence of $B_{c2}(T)$ at various pressures collapses into a universal curve and the comparison of $B_{c2}(T)$ to a polar-state function, implying exotic SC at lower pressures. A new CDW3 emerges just at $P_{c1} \approx 2.0$ GPa, and changes its behaviors at $P_{c2} \approx 4.50$ GPa accompanying a crossover from strong- to weak-coupling SC. Theoretical calculations proposed that the stronger interlayer coupling and band hybridization should be responsible for strong-coupling SC and that the coexisting weak-coupling SC and linear MR above 5 GPa is attributed to pressure-induced Lifshitz transitions.

[1] J. A. Wilson, F. J. Disalvo, and S. Mahajan, Charge-density waves in metallic, layered, transition-metal dichalcogenides, Phys. Rev. Lett. **32**, 882 (1974).

[2] C. A. Balseiro and L. M. Falicov, Superconductivity and charge-density waves, Phys. Rev. B **20**, 4457 (1979).

[3] G. Gruner, The dynamics of charge-density waves, Rev. Mod. Phys. **60**, 1129 (1988).

[4] B. Sipos, A. F. Kusmartseva, A. Akrap, H. Berger, L. Forró, and E. Tutiš, From Mott state to superconductivity in $1T$-TaS$_2$, Nat. Mater. **7**, 960 (2008).

[5] A. F. Kusmartseva, B. Sipos, H. Berger, L. Forro, and E. Tutis, Pressure induced superconductivity in pristine $1T$-TiSe$_2$, Phys. Rev. Lett. **103**, 236401 (2009).

[6] J. G. Bednorz and K. A. Müller, Possible high T_c superconductivity in the Ba-La-Cu-O system, Z. Phys. B **64**, 189 (1986).

[7] Y. Kamihara, T. Watanabe, M. Hirano, and H. Hosono, Iron-based layered superconductor La[O$_{1-x}$F$_x$]FeAs ($x = 0.05 - 0.12$) with $T_c = 26$ K, J. Am. Chem. Soc. **130**, 3296 (2008).

[8] E. Morosan, H. W. Zandbergen, B. S. Dennis, J. W. G. Bos, Y. Onose, T. Klimczuk, A. P. Ramirez, N. P. Ong, and R. J. Cava, Superconductivity in Cu$_x$TiSe$_2$, Nat. Phys. **2**, 544 (2006).

[9] S. I. Vedeneev, B. A. Piot, D. K. Maude, and A. V. Sadakov, Temperature dependence of the upper critical field of Bi$_2$Sr$_2$CuO$_x$ single crystals, Phys. Rev. B **60**, 12467 (1999).

[10] N. Kimura, K. Ito, H. Aoki, S. Uji, and T. Terashima, Extremely high upper critical magnetic field of noncentrosymmetric heavy fermion superconductor CeRhSi$_3$, Phys. Rev. Lett. **98**, 197001 (2007).

[11] H. Q. Yuan, J. Singleton, F. F. Balakirev, S. A. Baily, G. F. Chen, J. L. Luo, and N. L. Wang, Nearly isotropic superconductivity in (Ba,K)Fe$_2$As$_2$, Nature (London) **457**, 565 (2009).

[12] J. Jaroszynski, F. Hunte, L. Balicas, Y.-J. Jo, I. Raičević, A. Gurevich, D. C. Larbalestier, F. F. Balakirev, L. Fang, P. Cheng, Y. Jia, and H. H. Wen, Upper critical fields and thermally-activated transport of NdFeAsO$_{0.7}$F$_{0.3}$ single crystal, Phys. Rev. B **78**, 174523 (2008).

[13] B. S. Wang, Y. Liu, K. Ishigaki, K. Matsubayashi, J. Cheng, W. Lu, Y. Sun, and Y. Uwatoko, Pressure-induced bulk superconductivity in a layered transition-metal dichalcogenide $1T$-tantalum selenium, Phys. Rev. B **95**, 220501(R) (2017).

[14] J. J. Gao, J. G. Si, X. Luo, J. Yan, Z. Z. Jiang, W. Wang, Y. Y. Han, P. Tong, W. H. Song, X. B. Zhu, Q. J. Li, W. J. Lu, and Y. P. Sun, Origin of the large magnetoresistance in the candidate chiral superconductor $4H_b$-TaS$_2$, Phys. Rev. B **102**, 075138 (2020).

[15] A. Ribak, R. Majlin Skiff, M. Mograbi, P. K. Rout, M. H. Fischer, J. Ruhman, K. Chashka, Y. Dagan, and A. Kanigel, Chiral superconductivity in the alternate stacking compound $4H_b$-TaS$_2$, Sci. Adv. **6**, eaax9480 (2020).

[16] I. Silber, S. Mathimalar, I. Mangel, A. K. Nayak, O. Green, N. Avraham, H. Beidenkopf, I. Feldman, A. Kanigel, A. Klein, M. Goldstein, A. Banerjee, E. Sela, and Y. Dagan, Two-component nematic superconductivity in $4H_b$-TaS$_2$, Nat. Commun. **15**, 824 (2024).

[17] S. C. de la Barrera, M. R. Sinko, D. P. Gopalan, N. Sivadas, K. L. Seyler, K. Watanabe, T. Taniguchi, A. W. Tsen, X. Xu, D. Xiao, and B. M. Hunt, Tuning Ising superconductivity with layer and spin-orbit coupling in two-dimensional transition-metal dichalcogenides, Nat. Commun. **9**, 1427 (2018).

[18] Y. Liu, R. Ang, W. J. Lu, W. H. Song, L. J. Li, and Y. P. Sun, Superconductivity induced by Se-doping in layered charge-density-wave system $1T$-TaS$_{2-x}$Se$_x$, Appl. Phys. Lett. **102**, 192602 (2013).

[19] B. S. Wang, Y. Liu, X. Luo, K. Ishigaki, K. Matsubayashi, W. J. Lu, Y. P. Sun, J. -G. Cheng, and Y. Uwatoko, Universal phase diagram of superconductivity and charge density wave versus high hydrostatic pressure in pure and Se-doped $1T$-TaS$_2$, Phys. Rev. B **97**, 220504(R) (2018).

[20] K. T. Law and P. A. Lee, 1T-TaS$_2$ as a quantum spin liquid, Proc. Natl Acad. Sci. USA **114**, 6996 (2017).

[21] F. J. Disalvo, B. G. Bagley, J. M. Voorhoeve, and J. V. Waszczak, Preparation and properties of a new polytype of tantalum disulfide (4H_b-TaS$_2$), J. Phys. Chem. Solids **34**, 1357 (1973).

[22] I. Ekvall, J. J. Kim, and H. Olin, Atomic and electronic structures of the two different layers in 4H_b-TaS$_2$ at 4.2 K, Phys. Rev. B **55**, 6758 (1997).

[23] C. H.Wen, J. J. Gao, Y. Xie, Q. Zhang, P. F. Kong, J. H. Wang, Y. L. Jiang, X. Luo, J. Li, W. J. Lu, Y. P. Sun, and S. C. Yan, Roles of the narrow electronic band near the Fermi level in 1T-TaS$_2$-related layered materials, Phys. Rev. Lett. **126**, 256402 (2021).

[24] M. Tanaka, W. Mizutani, T. Nakashizu, S. Yamazaki, H. Tokumoto, H. Bando, M. Ono, and K. Kajimura, Study of charge-density waves in 4Hb-TaS$_2$ by STM/STS, Jpn. J. Appl. Phys. **128**, 473 (1989).

[25] R. M. Fleming and R. V. Coleman, Oscillatory magnetotransport in the layer compounds 4Hb-TaS$_2$ and 2H-TaSe$_2$, Phys. Rev. B **16**, 302 (1977).

[26] R. M. Fleming and R. V. Coleman, Oscillatory magnetoresistance in 4Hb-TaS$_2$, Phys. Rev. Lett. **36**, 1555 (1976).

[27] R. H. Friend, D. Jerome, R. F. Frindt, A. J. Grant, and A. D. Yoffe, Electrical conductivity and charge density wave formation in 4H_b-TaS$_2$ under pressure, J. Phys. C.: Solid State Phys. **10**, 1013 (1977).

[28] Y. Liu, L. J. Li, W. J. Lu, R. Ang, X. Z. Liu, and Y. P. Sun, Coexistence of superconductivity and commensurate charge density wave in 4H_b-TaS$_{2-x}$Se$_x$, J. Appl. Phys. **115**, 043915 (2014).

[29] S. X. Xu, Z. Y. Liu, P. T. Yang, K. Y. Chen, J. P. Sun, J. H. Dai, Y. Yin, F. Hong, X. H. Yu, M. Q. Xue, J. Gouchi, Y. Uwatoko, B. S. Wang, and J.-G. Cheng, Superconducting phase diagrams of S-doped 2H-TaSe$_2$ under hydrostatic pressure, Phys. Rev. B **102**, 184511 (2020).

[30] D. B. Mcwhan, R. M. Fleming, D. E. Moncton, and F. J. Disalvo, Reentrant lock-in transition of the charge-density wave in 2H-TaSe$_2$ at high-pressure, Phys. Rev. Lett. **45**, 269 (1980).

[31] D. B. Mcwhan, J. D. Axe, and R. Youngblood, Pressure-dependence of the striped-to-hexagonal charge-density-wave transition in 2H-TaSe$_2$, Phys. Rev. B **24**, 5391 (1981).

[32] J. A. Wilson, F. J. Di Salvo, and S. Mahajan, Charge-density waves and superlattices in the metallic layered transition metal dichalcogenides, Adv. Phys. **24**, 117 (1975).

[33] D. C. Freitas, P. Rodière, M. R. Osorio, E. Navarro-Moratalla, N. M. Nemes, V. G. Tissen, L. Cario, E. Coronado, M. García-Hernández, S. Vieira, M. Núñez-Regueiro, and H. Suderow, Strong enhancement of superconductivity at high pressures within the charge-density-wave states of 2H-TaS$_2$ and 2H-TaSe$_2$, Phys. Rev. B **93**, 184512 (2016).

[34] L. J. Li, X. Y. Deng, Z. Wang, Y. Liu, M. Abeykoon, E. Dooryhee, A. Tomic, Y. N. Huang, J. B. Warren, E. S. Bozin, S. J. L. Billinge, Y. P. Sun, Y. M. Zhu, G. Kotliar, and C. Petrovic, Superconducting order from disorder in 2H-TaSe$_{2-x}$S$_x$, npj Quantum. Mater. **2**, 11 (2017).

[35] C. G. Slough, W. W. McNairy, R. V. Coleman, B. Drake, and P. K. Hansma, Charge-density waves studied with the use of a scanning tunneling microscope, Phys. Rev. B **34**, 994 (1986).

[36] K. Y. Chen, N. N. Wang, Q. W. Yin, Y. H. Gu, K. Jiang, Z. J. Tu, C. S. Gong, Y. Uwatoko, J. P. Sun, H. C. Lei, J. P. Hu, and J.-G. Cheng, Double superconducting dome and triple enhance-

ment of T_c in the kagome superconductor CsV$_3$Sb$_5$ under high pressure, Phys. Rev. Lett. **126**, 247001 (2021).

[37] F. H. Yu, D. H. Ma, W. Z. Zhuo, S. Q. Liu, X. K. Wen, B. Lei, J. J. Ying, and X. H. Chen, Unusual competition of superconductivity and charge-density-wave state in a compressed topological kagome metal, Nat. Commun. **12**, 3645 (2021).

[38] J.-G. Cheng, K. Matsubayashi, S. Nagasaki, A. Hisada, T. Hirayama, M. Hedo, H. Kagi, and Y. Uwatoko, Integrated-fin gasket for palm cubic-anvil high pressure apparatus, Rev. Sci. Instrum. **85**, 093907 (2014).

[39] N. Mori, H. Takahashi, and N. Takeshita, Low-temperature and high-pressure apparatus developed at ISSP, University of Tokyo, High Pressure Res. **24**, 225 (2004).

[40] See Supplemental Material at http://link.aps.org/supplemental/10.1103/PhysRevB.109.144522 for crystal structure and electrical transport under various pressures of 4H_b-TaS$_2$ and DFT calculations.

[41] P. E. Blöchl, Projector augmented-wave method, Phys. Rev. B **50**, 17953 (1994).

[42] G. Kresse and D. Joubert, From ultrasoft pseudopotentials to the projector augmented-wave method, Phys. Rev. B **59**, 1758 (1999).

[43] G. Kresse and J. Furthmüller, Efficient iterative schemes for *ab initio* total-energy calculations using a plane-wave basis set, Phys. Rev. B **54**, 11169 (1996).

[44] G. Kresse and J. Furthmüller, Efficiency of ab-initio total energy calculations for metals and semiconductors using a plane-wave basis set, Comput. Mater. Sci. **6**, 15 (1996).

[45] J. P. Perdew, K. Burke, and M. Ernzerhof, Generalized gradient approximation made simple, Phys. Rev. Lett. **77**, 3865 (1996).

[46] H. J. Monkhorst and J. D. Pack, Special points for Brillouin-zone integrations, Phys. Rev. B **13**, 5188 (1976).

[47] J. Gao, Q. Wu, C. Persson, and Z. Wang, Irvsp: To obtain irreducible representations of electronic states in the VASP, Comput. Phys. Commun. **261**, 107760 (2021).

[48] J. Chen, J. L. Zhang, L. Jiao, Y. Chen, and H. Q. Yuan, Evidence for two-gap superconductivity in the non-centrosymmetric compound LaNiC$_2$, New. J. Phys **15**, 053005 (2013).

[49] A. I. U. Saleheen, R. Chapai, L. Y. Xing, R. Nepal, D. L. Gong, X. Gui, W. W. Xie, D. P. Young, E. W. Plummer, and R. Y. Jin, Evidence for topological semimetallicity in a chain-compound TaSe$_3$, npj Quantum Mater. **5**, 53 (2020).

[50] Y. Ando, Topological insulator materials, J. Phys. Soc. Jpn. **82**, 102001 (2013).

[51] E. Abarca Morales Sunko, I. Marković, M. E. Barber, D. Milosavljević, F. Mazzola, D. A. Sokolov, N. Kikugawa, C. Cacho, P. Dudin, H. Rosner, C. W. Hicks, P. D. C. King, and A. P. Mackenzie, Direct observation of a uniaxial stress-driven Lifshitz transition in Sr$_2$RuO$_4$, npj Quantum Mater. **4**, 46 (2019).

[52] J. Y. Kwon, M. Kim, D. J. Song, Y. Yoshida, J. Denlinger, W. Kyung, and C. Y. Kim, Lifshitz-transition-driven metal-insulator transition in moderately spin-orbit-coupled Sr$_{2-x}$La$_x$RuO$_4$, Phys. Rev. Lett. **123**, 106401 (2019).

[53] T. Nishimura, H. Sakai, H. Mori, K. Akiba, H. Usui, M. Ochi, K. Kuroki, A. Miyake, M. Tokunaga, Y. Uwatoko, K. Katayama, H. Murakawa, and N. Hanasaki, Large enhancement of thermoelectric efficiency due to a pressure-induced Lifshitz transition in SnSe, Phys. Rev. Lett. **122**, 226601 (2019).

[54] K. Ma, K. Gornicka, R. Lefèvre, Y. Yang, H. M. Rønnow, H. O. Jeschke, T. Klimczuk, and F. O. von Rohr, Superconductivity

with high upper critical field in the cubic centrosymmetric η-carbide $Nb_4Rh_2C_{1-\delta}$, ACS Mater. Au **1**, 55 (2021).

[55] V. G. Kogan and R. Prozorov, Orbital upper critical field and its anisotropy of clean one- and two-band superconductors, Rep. Prog. Phys. **75**, 114502 (2012).

[56] L. F. Shi, B. B. Ruan, P. T. Yang, N. N. Wang, P. F. Shan, Z. Y. Liu, J. P. Sun, Y. Uwatoko, G. F. Chen, Z. A. Ren, B. S. Wang, and J.-G. Cheng, Pressure-driven evolution of upper critical field and Fermi-surface reconstruction in the strong-coupling superconductor Ti_4Ir_2O, Phys. Rev. B **107**, 174525 (2023).

[57] W. L. McMillan, Transition temperature of strong-coupled superconductors, Phys. Rev. **167**, 331 (1968).

[58] C. Pfleiderer, Superconducting phases of f-electron compounds, Rev. Mod. Phys. **81**, 1551 (2009).

[59] Y. P. Li, C. An, C. Q. Hua, X. L. Chen, Y. G. Zhou, Y. Zhou, R. R. Zhang, C. Y. Park, Z. Wang, Y. H. Lu, Y. Zheng, Z. R. Yang, and Z.-A. Xu, Pressure-induced superconductivity in topological semimetal $NbAs_2$, npj Quantum Mater. **3**, 58 (2018).

[60] B. Shen, X. Y. Deng, G. Kotliar, and N. Ni, Fermi suface topology and negative longitudinal magnetoresistance obserbed in the semimetal $NbAs_2$, Phys. Rev. B **93**, 195119 (2016).

[61] S. M. Nie, L. Xing, R. Y. Jin, W. W. Xie, Z. J. Wang, and F. B. Prinz, Topological phases in the $TaSe_3$ compound, Phys. Rev. B **98**, 125143 (2018).